Science and Technology for Energy Transition **79**, 35 (2024)

https://doi.org/10.2516/stet/2024029

Power Components For Electric Vehicles
Hamid Ben Ahmed, Yacine Amara and Mohamed Gabsi (Guest Editors)

Available online at:
stet-review.org

REGULAR ARTICLE

OPEN ACCESS

Real-time simulation of a new design of a smart and fast electric vehicle charger

Hanen Messaoudi[1,*], Manef Bourogaoui[1,2], and Afef Bennani-Ben Abdelghani[1,3]

[1] Université Tunis El Manar, Ecole Nationale d'Ingénieurs de Tunis, LR11ES15, Laboratoire des Systèmes Electriques, 1002 Tunis, Tunisia
[2] Institut Supérieur des Technologies de l'Information et de la Communication, Université de Carthage, Tunis, Tunisia
[3] Institut National des Sciences Appliquées et Technologie, INSAT, Université de Carthage, 1080 Tunis, Tunisia

Received: 22 September 2023 / Accepted: 19 April 2024

Abstract. Due to the growing global adoption of electric vehicles (EVs), there is a pressing demand for the development of charging infrastructure that offers enhanced performance while reducing the charging time of EVs. Combining innovative fast and smart charging technologies can result in cost-efficient charging solutions, optimized energy exploitation, and reduced charging time for EVs. This paper proposes a new design of a smart and fast charger for EV batteries. The charger is made of a PFC-based Vienna Rectifier (VR) and an isolated Dual Active Bridge (DAB) converter. The proposed charger enables intelligent data flow between the battery and the charger thanks to the Controller Area Network (CAN) communication employed by the CHAdeMO charging protocol. To validate the effectiveness and feasibility of the proposed charger, the results of real-time simulations performed on RT-LAB platform, from OPAL-RT are presented and discussed.

Keywords: Electric Vehicles, Fast battery charging, Smart CAN communication, PFC-based Vienna rectifier, Real-time simulation, RT-LAB platform.

1 Introduction

Over 30% of the atmospheric particle emissions worldwide are caused by transportation [1]. Climate change affects the environment and biodiversity of this planet due to the enormous rise in pollution from fossil fuels. Consequently, governments and organizations worldwide have implemented severe emission standards for both new and used vehicles to mitigate automobile exhaust emissions [2]. Since it is impossible to completely eliminate emissions from fossil fuel-powered vehicles, automakers are attempting to electrify transportation. Therefore, automakers are increasingly focusing on electrifying transportation. Distinguished EV manufacturers like Toyota, Tesla, Nissan Leaf, and Ford are heavily investing in the development of EV charging systems to sustain their growth in the coming years [3]. This shift has motivated the evolution of innovative EV technologies since the 2010s [4, 5] and research works in fast and ultrafast charging systems and technologies have emerged, thanks to advancements in battery technology, power electronics, and control systems [6].

In the domain of EV charger design, power converters are critical operational and control units [7–9]. Hence, when designing EV chargers, it is crucial to consider optimal structural design, safety measures, high efficiency, and fast charging capabilities [3, 10, 11] depending on the application and battery specifications [12, 13].

The first power stage of a charger involves the AC/DC converter, directly linked to the public grid. This stage enhances power quality at the AC inputs, reduces Total Harmonic Distortion (THD), and mitigates Electromagnetic Interference (EMI) noise. Consequently, a range of designs employing various AC/DC converter configurations and control strategies have been proposed [14–16]. For instance, [17] introduced a three-phase buck-type rectifier that offers high efficiency, power density, and low THD. In contrast [18] presented a three-phase boost-type rectifier with Power Factor Correction (PFC) control. Despite their advantages, the THD of boost and buck-type rectifiers remains relatively high compared to alternatives like the Vienna Rectifier (VR) [19]. Sweety *et al.* [20] introduced a VR based on PFC control for EV charging stations, a topology favored for high-power applications due to its high-power density, simple control, high efficiency, very low THD, fewer switches, and unity power factor [21–23].

* Corresponding author: hanen.messaoudi@enit.utm.tn

Therefore, it is widely employed in various applications that require high-quality DC power supply, such as battery chargers [24]. Multistage converters are also widely adopted in charger designs due to their efficiency and power density under high-power conditions [25, 26].

DC/DC converters, representing the second power stage in charger designs, are directly tied to the vehicle's battery. EV battery charging systems have utilized several non-isolated and isolated DC/DC converters [16]. Deng *et al.* [27], for example, proposed an LLC resonant DC/DC converter known for high power density, efficiency, and low EMI noise, though its design and analysis are intricate. Meanwhile, Dual Active Bridge (DAB) converters have become increasingly popular in EV battery chargers [28–30] due to their notable advantages.

The DAB topology consists of two full-bridge DC/AC converters, a high-frequency isolation transformer with a leakage inductor that accounts for any external energy transfer inductance and encompasses the transformer's leakage properties. Notably, the DAB converter offers high-frequency isolation, enabling effective power transfer with minimal magnetic size and weight. It supports bidirectional power flow and efficiently regulates and transforms voltage levels, which is crucial for aligning the grid voltage with EV battery charging requirements [31]. Furthermore, the DAB converter's topology can reduce electromagnetic interference, assisting compliance with regulatory electromagnetic compatibility (EMC) standards.

Moreover, DAB converters exhibit high efficiency, contributing to the overall energy efficiency of the charging system. They also boast higher power density compared to traditional converters, making them suitable for compact, high-power applications like fast chargers [32]. Ongoing research in DAB technology focuses on advancements such as sophisticated control algorithms, fault-tolerant features, and improved thermal management, aiming to optimize the performance and reliability of DAB-based EV fast chargers.

In brief, the adoption of DAB technology in EV battery fast chargers is driven by its capacity to provide high-frequency isolation, bidirectional power flow, efficiency, and flexibility. As the demand for swift and efficient charging solutions rises, DAB converters are prepared to play a significant role in shaping the future of EV charging infrastructure. Their application extends to various applications, thanks to advancements in semiconductor technology using SiC and GaN-based devices [23, 33]. This topology operates at a fixed switching frequency and employs small passive components, controlled via zero-voltage switching (ZVS) to obtain sinusoidal waveforms in the DAB's DC-DC stage by adjusting the phase shift between primary and secondary voltages.

In summary, creating an optimal EV battery charger structure necessitates selecting suitable power converter topologies and control strategies that align with specific applications and battery characteristics. Numerous factors and constraints must be carefully considered during the design process, covering weight, cost, size, power losses, isolation, voltage and current requirements, battery specifications, and charger efficiency. For instance, an increased number of power switches in a converter can increase overall cost, size, and complexity. Conversely, reducing power switches may require additional components like EMI filters, power factor correction (PFC) controllers, and snubbers, which can also raise costs and size. Alternatively, size reduction can be achieved by increasing the operating frequency, but this may introduce electromagnetic interference (EMI) issues [9].

Given the ongoing research and available literature, this paper proposes a fast and smart charger for a Lithium-Ion (Li-Ion) EV battery. Li-Ion batteries are widely recognized energy storage technology known for their higher energy density compared to conventional lead-acid or nickel-cadmium batteries, resulting in a more compact form factor. Additionally, Li-Ion batteries are chosen for their safety advantages, making them a preferred choice for EVs [34].

The design and sizing of the proposed battery charger were conducted using MATLAB/Simulink®. It consists of a VR controlled by a hysteresis regulator on the AC side and a DAB and a Buck converter controlled by a Constant Current Constant Voltage (CCCV) algorithm on the battery side.

Regarding charging speed, we employ a Mode 4 charging approach, offering DC charging capabilities exceeding 150 kW, suitable for public and commercial applications [35]. Specifically, we adopt the CHAdeMO charging protocol with a Power Class 1.0 rating, delivering a maximum output power of 62.5 kW (at 500V and 125A) [36]. CHAdeMO is a well-established charging system known for its advanced and mature technology, originating in Japan. When charging at 50 kW, it can charge a battery to 80% capacity in just 30 min [37]. Additionally, the CHAdeMO protocol facilitates intelligent data transfer between the EV battery and the charging point using the Controller Area Network (CAN) communication protocol, ensuring rapid, safe, secure, and efficient charging operations.

We conducted simulation tests using MATLAB/Simulink® under various charging scenarios. The results demonstrate that our proposed fast charger can fully charge the EV battery in under 30 min while maintaining a pure sinusoidal input current.

Furthermore, we validated the effectiveness and proper operation of our proposed charger through real-time simulation tests using RT-LAB platform, from OPAL-RT. RT-LAB platform is a real-time simulator fully compatible with MATLAB/Simulink®, bringing about a significant transformation and performance enhancement in the world of model-based design [38]. The real-time simulator incorporates essential tools, including the Real-Time Distributed Simulation Package (RT-LAB) and algorithmic toolboxes. RT-LAB executes Simulink® block diagrams on a PC-Cluster, while the algorithmic toolboxes facilitate the design of complex electrical circuits and their controllers.

The paper is organized as follows: Section 2 details the design of the proposed fast and smart charger, providing a thorough description of its power stage components and control methods. Section 3 discusses the utilization of CAN communication for intelligent data exchange between the charger and the battery. In Section 4, we showcase and analyze the simulation results obtained through MATLAB.

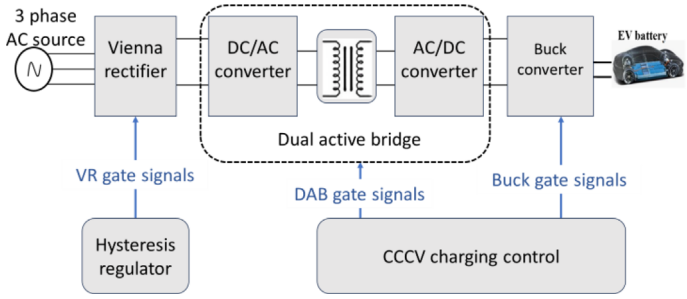

Fig. 1. Proposed smart and fast EV charger block diagram.

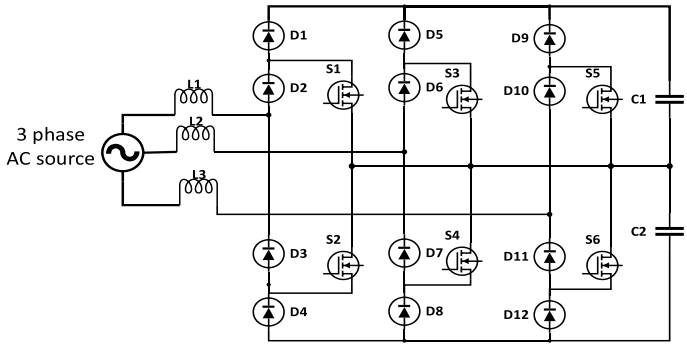

Fig. 2. Vienna rectifier circuit.

Finally, Section 5 outlines the implementation of the system on the RT-LAB simulator and presents the real-time simulation results.

2 Proposed charger configuration

The proposed design for a fast and smart charger enables the conversion of a 3-phase symmetrical 400 V_{rms} line-to-line AC grid voltage into the required DC battery voltage. To ensure quick, reliable, secure, and efficient charging [39], the sizing of the charging system must meet several fundamental criteria, taking into account factors like battery capacity, charging duration, and the desired charging rate.

It is worth mentioning that this study does not incorporate considerations for power losses associated with the switches during the design and sizing of the charging system.

Figure 1 illustrates the block diagram of the proposed charging system.

2.1. Power stage configuration

The charger's power stage comprises two components: a grid-side AC/DC converter employing a Vienna Rectifier and a controlled battery charging unit that includes an isolated bidirectional DAB converter and a buck converter.

Effective communication between the charger and the EV battery is achieved through the use of the Controller Area Network (CAN) communication protocol as part of the CHAdeMO charging standard.

2.1.1 Vienna rectifier

A three-phase unidirectional VR is employed to transform the AC grid voltage into a regulated DC voltage. The choice and sizing of the VR consider various essential factors, such as achieving unity power factor and maintaining high power quality on the AC side, ensuring controllability of the DC voltage, keeping the structure explicit, and managing costs effectively. The configured three-phase VR topology is depicted in Figure 2.

The VR circuit is composed of three inductors (L_1, L_2, L_3) on the input AC grid side, three power legs for the three phases, and two connected output capacitors (C_1 and C_2) in series on the DC link. This converter allows power to flow in one direction only. Each power leg comprises four high-voltage-resistant rectifier diodes capable of withstanding voltages as high as 1000 V and two reverse-connected MOSFETs that can operate at very high frequencies, reaching up to a few MHz, and endure high voltages of up to 2 kV [9].

The intended ripple in line current is determined by the values of inductors L_1, L_2, and L_3, and it is computed using the below equation:

$$\Delta_{\text{ipp}} = \frac{V_{\text{DC}} \times 0.5 \times T_{\text{s}}}{4 \times L_{a,b,c}} \tag{1}$$

$T_{\text{s}} = \frac{1}{f_{\text{sw-VR}}}$ is the switching period, $f_{\text{sw-VR}}$ is the switching frequency of the VR, and V_{DC} is the DC bus voltage.

Certainly, decreased current ripple values can alleviate strain on the battery, potentially prolonging its lifespan. As indicated by equation (1), augmenting the inductance

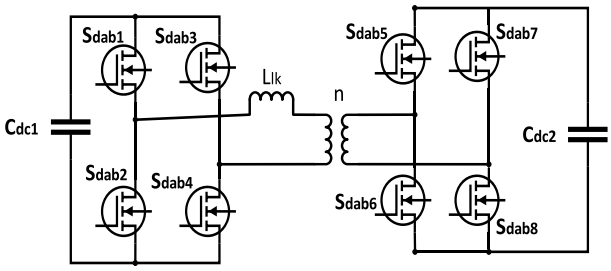

Fig. 3. Bidirectional isolated DAB topology.

values can indeed lead to a reduction in the current ripple. Additionally, reducing the output capacitor size can result in a more compact design with higher power density.

In terms of the control strategy employed for the VR in this study, a hysteresis-based controller was chosen. Hysteresis control is a widely adopted and efficient technique for power electronics converters due to its ability to deliver swift dynamic responses and robust performance.

2.1.2 Dual Active Bridge (DAB) converter

The DAB converter configuration is depicted in Figure 3. The converter is made of identical primary and secondary side full bridges, a high-frequency isolation transformer with a turn ratio denoted as n, a leakage inductor L_{lk}, and two DC bus capacitors, namely, C_{dc1} and C_{dc2}.

Each full bridge's two legs are controlled with complementary square-wave pulses. The DAB converter allows for directed power flow by adjusting the phase of pulses in one bridge relative to the other through phase-shift modulation. The phase shift, denoted as φ, between the primary and secondary voltages' fundamentals plays a crucial role in this control strategy. This approach effectively manages power transfer between the two DC buses, ensuring that the leading bridge transmits power to the lagging bridge. The application of square waves to the bridges induces a voltage difference across the leakage inductance, thus guiding the flow of stored energy.

2.1.3 Buck converter

This is a step-down converter designed to produce an average output voltage V_{Buck} that is lower than its input voltage V_{in}. The buck converter is responsible for directly charging the EV battery and consists of a single switching cell comprising a single MOSFET and a single diode. The circuit of the buck converter is shown in Figure 4.

The buck output voltage is calculated by equation (2).

$$V_{\mathrm{buck}} - V_{\mathrm{in}} \times \frac{T_{\mathrm{ON}}}{T}. \tag{2}$$

T is the switching period of the MOSFET and T_{ON} is the duration of its ON state.

2.2 Control strategy

2.2.1 Hysteresis regulator

To regulate the AC side current, a hysteresis current controller is employed to control the VR. This approach

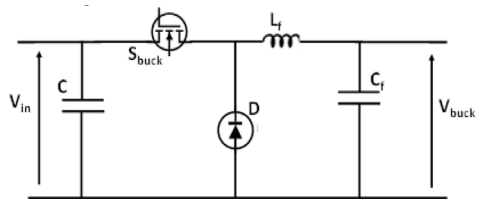

Fig. 4. Buck converter circuit.

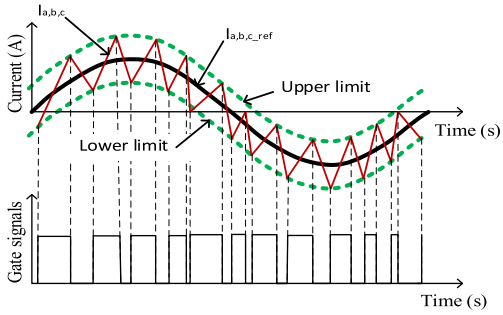

Fig. 5. Hysteresis current controller principle.

guarantees that the input current waveform remains sinusoidal. Its effectiveness lies in its remarkable dynamic capabilities, enabling rapid responses to sudden shifts in the reference current [40]. Moreover, its design is characterized by its simplicity and robustness, eliminating the need for intricate analysis. However, it is important to note an important drawback of this controller: Its switching frequency is variable and heavily reliant on both the load parameters and the specific system requirements.

The principle of a hysteresis current controller is shown in Figure 5. It is based on the controlled value ($i_{\mathrm{a,b,c}}$), its reference ($i_{\mathrm{a,b,c\_ref}}$), and the predefined upper and lower limits which it must follow. Both limits create the hysteresis band. The error, calculated as the difference between the reference value and the measured one, should fall within the upper and lower limits. The gate signals generated for the VR are then the results of the comparison of this error and the controller's upper and lower limits.

2.2.2 CCCV charging control

The charging process of a Lithium-ion battery is shown in Figure 6.

It is characterized by two main phases: Constant current (CC) and Constant Voltage (CV). In the initial phase, often referred to as the CC phase or bulk mode, the battery undergoes charging with a substantial and unchanging current, commonly known as the bulk current. This phase persists until the battery's Open Circuit Voltage (OCV) is attained. Subsequently, the charging transitions into the CV phase, also known as the absorption mode. During this phase, a constant voltage equal to the battery's OCV is maintained across the battery terminals. As a result, the charging current gradually diminishes until it reaches a predetermined level known as the float value. The charging process is considered complete when the

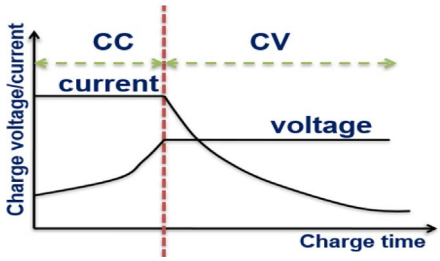

Fig. 6. Lithium-ion battery charging curve.

current drops below this float value threshold, indicating that the battery is fully charged. The CCCV charging algorithm is widely adopted in fast charger designs due to its ability to mitigate thermal stress and prevent overvoltage [9, 41, 42].

Figure 7 illustrates the principle of the CCCV algorithm in a flowchart format.

The CCCV control algorithm relies on two crucial parameters: the SOC_{limit} set at 95% and the SOC_{thresh} at 80%. In this system, the CC mode manages the DAB converter, while the CV mode governs the Buck Converter. The DAB converter takes charge of the phase shift control, and power flow control within the DAB converter is accomplished using a conventional power transfer method. To generate a high-frequency AC square waveform at the primary inductive coil of the transformer, a bipolar switching technique is employed with a duty cycle of 0.5.

3 Smart charger/battery communication

The sequence of the charging process is determined by the chosen protocol and charging method. In this work, the CHAdeMO protocol is employed to facilitate data exchange between the battery and the charger. The CHAdeMO connector enables both analog signal transmission and digital communication via the Controller Area Network (CAN). CAN is a robust vehicle bus standard that enables communication between the microcontroller, which houses the control algorithms, and the EV battery [43]. To depict the optimal interaction between the EV owner and the charging system, a charging sequence diagram, as shown in Figure 8, was created using StarUML software.

Throughout the charging process, two software components, the Charge Control Stack (CCS) and the station web backend, engage in direct interaction. The start of the charging process begins when the EV owner plugs their vehicle in, inserting the connector into the appropriate outlet at the charging station. This action triggers a signal from the connector to the CCS, which in turn commands the connector to lock securely in place. The system confirms successful vehicle connection by securing the connector. Subsequently, the owner selects their preferred charging method and completes any required authentication steps. Once authenticated, CCS marks authorization as "true," and a confirmation message signals the commencement of charging. Following this confirmation, the EV assesses the current level based on battery performance and prevailing

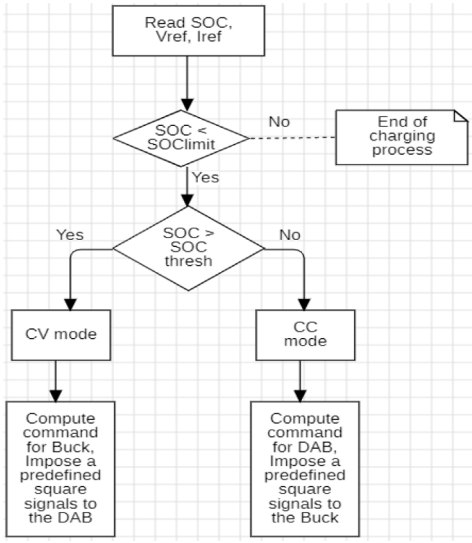

Fig. 7. CCCV control algorithm.

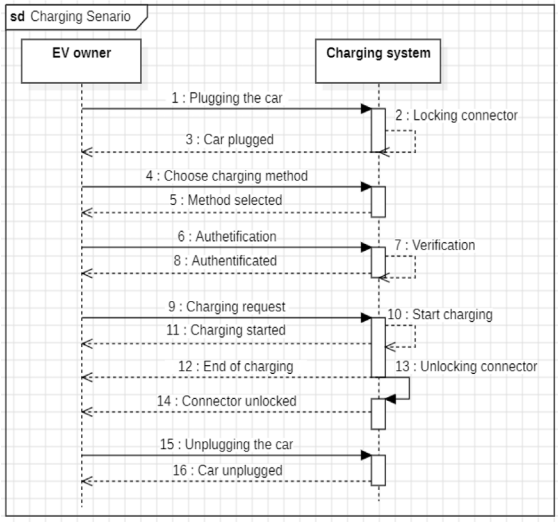

Fig. 8. Charging sequence diagram.

conditions, allowing the battery charging process to begin. The current level is continuously relayed to the charger via the CAN bus every 0.1 s.

Upon reaching a full charge, the EV sends zero current signals via the CAN bus. In response, the charger discontinues power supply to prevent overcharging, and the CCS notifies the web backend system to instruct the outlet to release the connector. The user is alerted to the completion of the charging task through the touchscreen, thanks to a signal transmitted by the web backend. This signal indicates that it is safe to disconnect their vehicle.

4 System configuration and control

Simulation tests conducted using MATLAB/Simulink® serve to confirm the efficiency of the proposed EV charger.

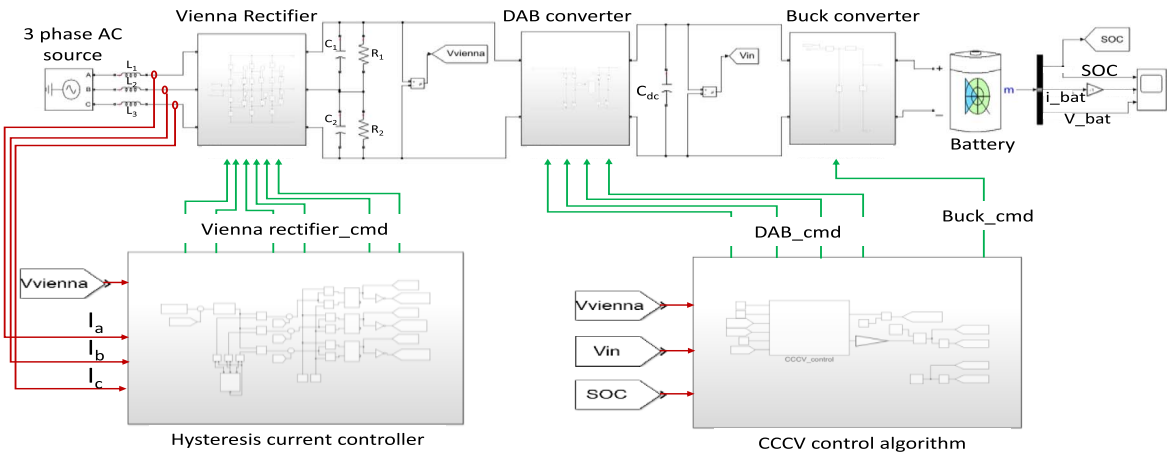

Fig. 9. Proposed charger circuit on Simulink.

The battery under consideration is a 66.2 Ah Nissan Leaf model from 2010, featuring a nominal voltage of 360 V. The implemented proposed charger circuit and the adopter control on Simulink are depicted in Figure 9. The generic battery model of Simulink is used to implement this charging system.

4.1 Implemented hysteresis current controller

In this study, we opted to implement a detailed circuitry for the hysteresis comparator to generate the gate signals for the VR instead of utilizing the Simulink hysteresis comparator block, which only requires upper and lower limit configuration. This choice allows us to illustrate the specific steps required to generate the desired gate signals for the VR switches.

The hysteresis comparator circuit consists of comparing a voltage reference equal to 800 V, indicating the desired DC voltage the VR will produce, to the measured value Vienna. The error from this comparison undergoes correction through a PI corrector. The corrected error is then multiplied by the three reference currents measured from a three-phase source with a line-to-line value equal to 1. These references serve as the baseline for our measured currents $I_{a,b,c}$. After subtracting each reference from the corresponding measurement, the error is compared with the predetermined upper and lower limits, set at 1 and −1, respectively. The compared error values with the upper and lower limits are connected to three Set-Reset Flip Flops. The Q output generates square signals for each pair of MOSFETs within the Boost PFC blocks of the VR.

4.2 Implemented CCCV control algorithm

As depicted in Figure 7, in CC mode ($\mathrm{SOC} < \mathrm{SOC}_{\mathrm{thresh}}$, $\mathrm{SOC}_{\mathrm{thresh}} = 80\%$), the DAB converter takes charge of phase shift control. To regulate power flow through the DAB converter, a bipolar switching technique is employed with a 50% duty cycle, generating a high-frequency AC square wave at the primary inductive coil. For power transfer, switching pulses from the primary are phase-shifted by an angle $d = \frac{\varphi}{\pi}$ and then applied to the secondary side. The phase shift angle can be determined by solving the quadratic equation provided in equation (3).

$$\frac{d^2 - d + 2 \times L_{\mathrm{lk}} \times I_{\mathrm{ref}}}{n \times V_{\mathrm{Vienna}} \times T_{\mathrm{s}}}. \tag{3}$$

Here, $T_{\mathrm{s}} = \frac{1}{f_{\mathrm{s}}}$ represents the switching period, L_{lk} is the leakage inductance, V_{Vienna} is the VR output voltage, n is the turns ratio of the primary to secondary coils, and I_{ref} is the bulk current. The positive roots of the equation are selected as the solution. Once the phase shift is calculated, it needs to be converted from degrees to seconds through a gain block equal to $\frac{T_{\mathrm{s}}}{360}$. Subsequently, a variable time delay block is responsible for applying the phase shift to a square waveform ultimately generating the gate signals for the secondary bridge of the DAB. The gate signals for the primary bridge are generated using a straightforward square waveform block.

In CV mode, ($\mathrm{SOC} < \mathrm{SOC}_{\mathrm{thresh}}$) when the transition is made from CC to CV mode, the constant voltage control loop assured by the buck converter is activated. The buck converter is controlled using a Pulse Width Modulation (PWM) technique, and its reference α is computed within the constant voltage control loop according to equation (4).

$$\alpha = \frac{V_{\mathrm{Buck}}}{V_{\mathrm{in}}} \tag{4}$$

Table 1. Specific parameters of the charger components.

Parameter	Value	Parameter	Value
P	62.5 kW	V_{in}	400 V (AC)
V_{dc}	800 V	I_{ref}	125 A
f_{s}	10 kHz	n	1
L_{lk}	$10\mathrm{e}^{-6}$ H	C_{dc}	$4\mathrm{e}^{-4}$ F
$L_{\mathrm{a,b,c}}$	3,125 mH	$C_{1,2}$	5 mF
L_{f}	13. 5 mH	C_{f}	3 μF

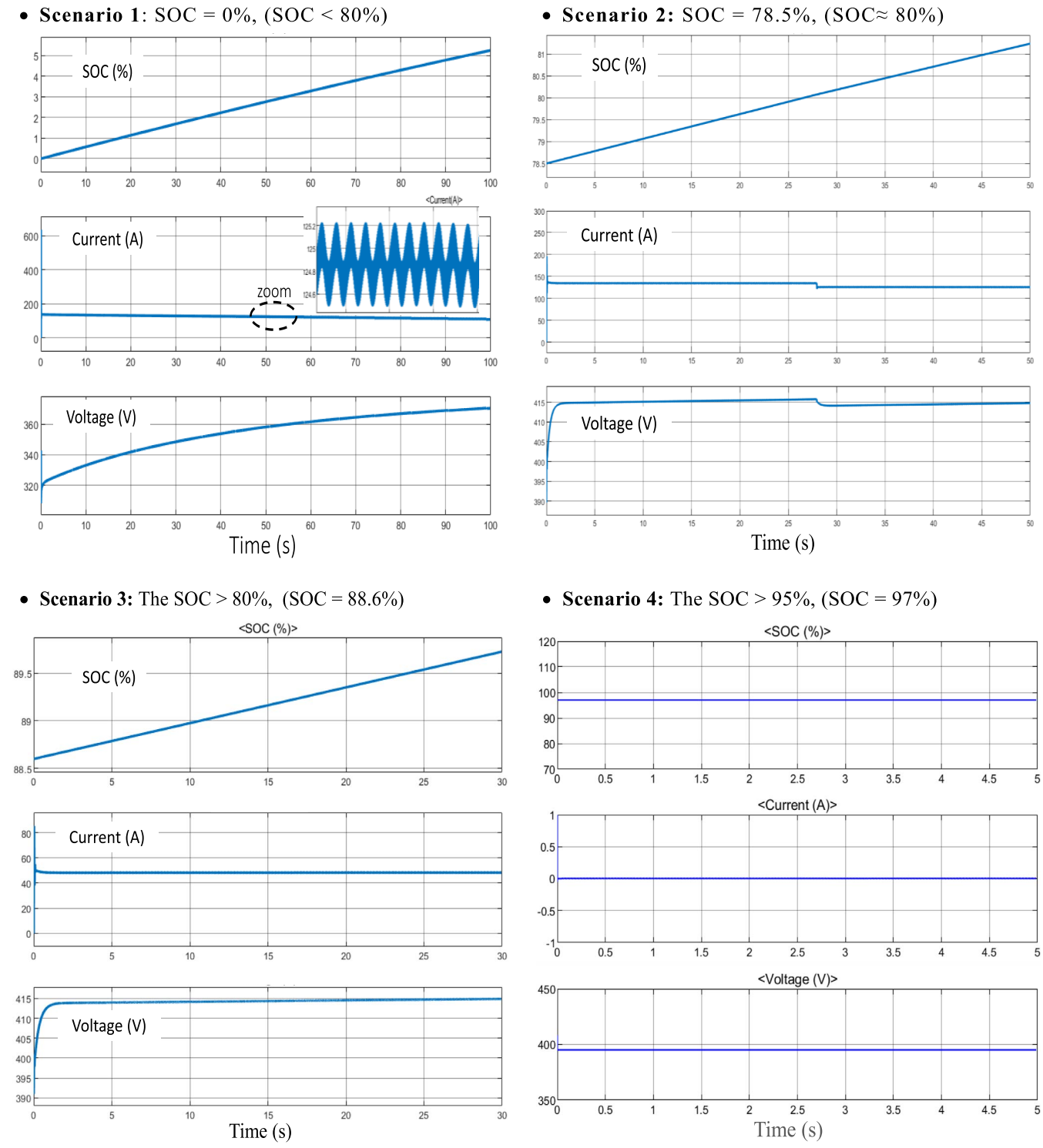

Fig. 10. Battery SOC (a), current (b) and voltage (c) curves for four scenarios.

The specific parameters of the proposed charger structure are depicted in Table 1.

The charging control algorithm launches the battery charging process with a bulk current set at 125 A. Subsequently, it switches to a constant voltage of 415 V during the absorption phase.

4.3 Simulation results and discussion

In this study, we simulate four charging scenarios, each starting with varying initial State of Charge (SOC) values. The results obtained for the battery's SOC, current, and voltage for each scenario are presented in Figure 10.

In Scenario 1 (SOC < 80%), when the battery starts with a 0% charge, it operates in the CC mode. During this phase, the battery's current remains steady at 125 A, and the voltage gradually rises from 320 V to reach 370 V over 100 s, as depicted in Figure 10. The current exhibits a ripple of approximately 0.5 A. By the conclusion of this phase, the battery SOC reaches 5%.

For Scenario 2 (SOC ≈ 80%), the battery voltage begins at roughly 415 V and undergoes a gradual rise, reaching 417 V. The charging mode transitions from CC to CV mode at approximately 29 s. Meanwhile, the SOC increases from 78.5% to approximately 81% (around 80%).

During this transition, there is a brief temporary drop in voltage before it swiftly returns and stabilizes at the 415 V level. Throughout this 50-second phase, the current experiences a gradual drop, declining to 105 A.

Figure 10 describing Scenario 3 (SOC > 80%) shows that the battery undergoes a charging process, raising its SOC from 88.6% to 89.2% within 30 s. The process begins with an initial voltage of 400 V and quickly stabilizes at the desired 415 V. Throughout this period, the current is consistently maintained at around 50 A, although steadily decreasing over time.

In Scenario 4 (SOC > 95%), the SOC exceeds the predefined SOC_{limit}. As a result, the current drops to 0 A, and the voltage hovers around 394 V, indicating the completion of the charging process. This phase continues for 5 s.

The simulation results confirm the effectiveness and proper functioning of the proposed fast and smart battery charger, along with the adopted control design. Notably, it demonstrates the charger's capability to complete the charging process in under 30 min.

To further validate the system's performance, the outcomes of real-time simulations conducted using the real-time environment of RT-LAB platform, from OPAL-RT are also presented.

5 Digital implementation of the real-time simulation using RT-LAB platform, from OPAL-RT (OP4510)

The OPAL RT (OP4510) simulator is used for the real-time simulation of the proposed system. Indeed, the hardware offers a real-time platform called RT-LAB and eFPGAsim, which integrates multicore CPU along with FPGA chips. It is characterized by the following features:

- Model: (OP4510-1) High-performance in real-time.
- Real-time system: Linux REDHAT.
- FPGA: Kintex-7 FPGA.
- Computer: 8GB RAM, Xeon E3 core CPU, 3.3 GHz.
- Four I/O boards: 16 analog inputs, 16 analog outputs, 32 digital inputs, 32 digital outputs.
- Connectors: DB37 (used for connector synchronization).

In this work, the proposed charger is implemented using a time step of 5 µs. This time step allowed the system, along with its control algorithm, to be executed entirely on the CPU core of the hardware target without experiencing overruns. The real-time simulation environment established in the laboratory is shown in Figure 11.

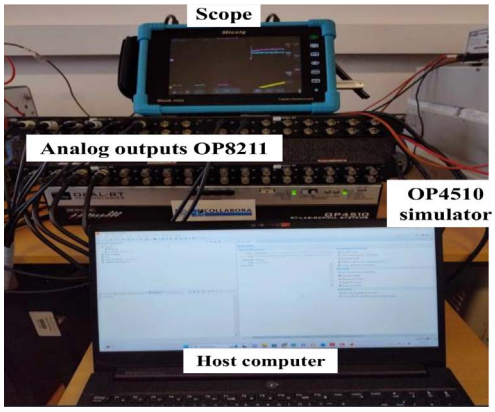

Fig. 11. Real-time simulation test bench.

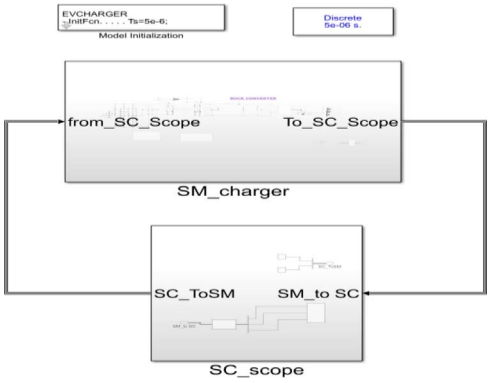

Fig. 12. Basic communication link between SM and SC subsystems.

The host computer is employed to interact with the graphical user interface generated after compiling the Simulink model set up on RT-LAB. Communication between the host computer and the real-time simulator OP4510 is ensured through an Ethernet cable. A scope is utilized for visualizing signals.

To run the developed MATLAB/Simulink® charger model on the OP4510 simulator, it needs to be divided into two subsystems, as depicted in Figure 12. There is a Master subsystem (SM) containing the complete Simulink model and a Console subsystem (SC) that includes all the scopes and displays.

The details of the Master subsystem and the Consol subsystem are depicted in Figure 13.

The real-time simulation results are presented in Figure 14, showing the waveforms of the State of Charge (SOC), battery voltage (V_{bat}), and current (I_{bat}).

The simulation starts with an initial SOC of 0% and reaches 95%, which is the SOC_{limit}. The graph covers approximately 30 min of the charging process. During the CC mode, the SOC remains below 80%, with a constant

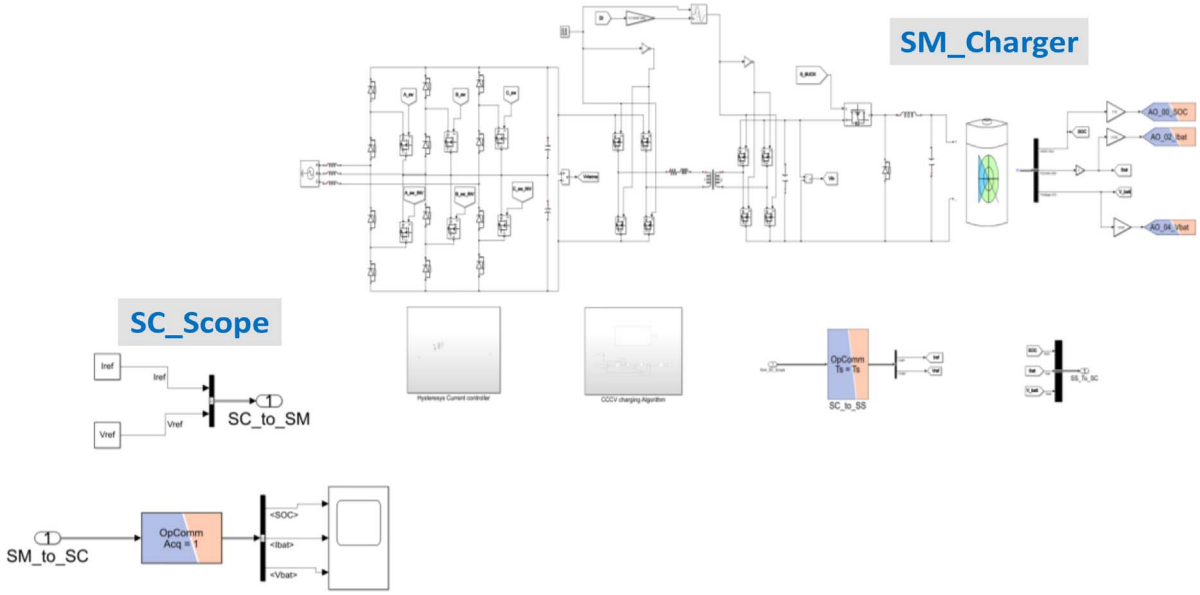

Fig. 13. SM and SC subsystem details.

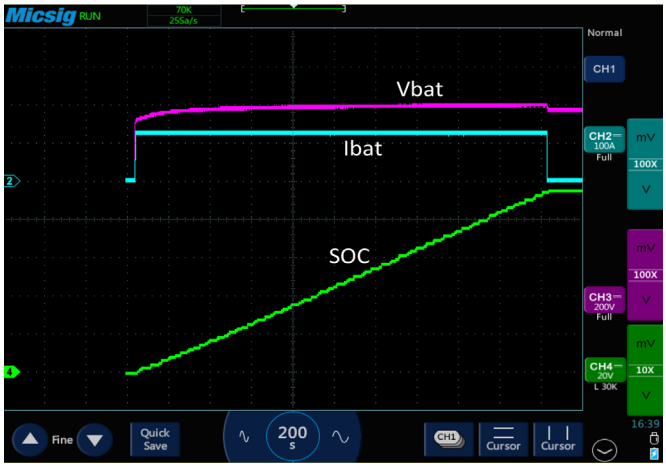

Fig. 14. Real-time simulation Li-Ion battery charging process.

current of 125 A and a voltage steadily increasing from 320 V to 370 V. In the second phase, when the SOC reaches 80%, the current remains approximately constant at 125 A, and the voltage stabilizes at around 415 V.

The real-time simulation result does not show the transition from CC to CV mode due to the scope's time rating being set to 200 s/div to display the entire 30-minute charging period. The charging stops once the battery SOC reaches 95%, with the current decreasing to zero and the voltage stabilizing at 394 V.

Based on the real-time simulation results displayed above, it is obvious that they are in excellent agreement with the simulation outcomes obtained from MATLAB. This assent serves as further confirmation of the successful operation of the proposed battery charger.

6 Conclusion and perspectives

This paper introduces, designs, and simulates a smart and rapid EV battery charger. The charger's design emphasizes fast, secure, and efficient charging operations, The proposed charger design consists of a VR controlled using a hysteresis regulator and a DAB followed by a buck converter regulated by a Constant Current Constant Voltage algorithm on the battery side.

The use of the CHAdeMO charging protocol in this study facilitates intelligent data exchange between the charger and the battery using the CAN communication protocol.

Simulation tests conducted on MATLAB/Simulink® and validated using the real-time environment of the RT-LAB platform with a fixed step affirm the efficiency and the proper operation of the proposed power and control design, as it ensures high power quality with minimal current ripple and achieves battery charging in under 30 min. Accordingly, the real-time simulator shows promising potential for the design and testing of Electric Vehicle battery models, simultaneously enhancing the overall performance of the developed model.

Following the successful real-time simulation, the next step in this study is to experimentally validate the proposed battery charger structure and control. Figure 15 illustrates the experimental test bench equipment available in our laboratory, which we will utilize for this purpose. We plan to employ Power Hardware-in-the-Loop (PHIL) for the experimental validation.

Specifically, the electrical circuit of the proposed power conversion topology will be implemented in Hardware-in-the-Loop (HIL) using the Electric Hardware Solver (eHS) of the OP4510 real-time simulator. In this setup, the converter will be implemented in the FPGA board of the

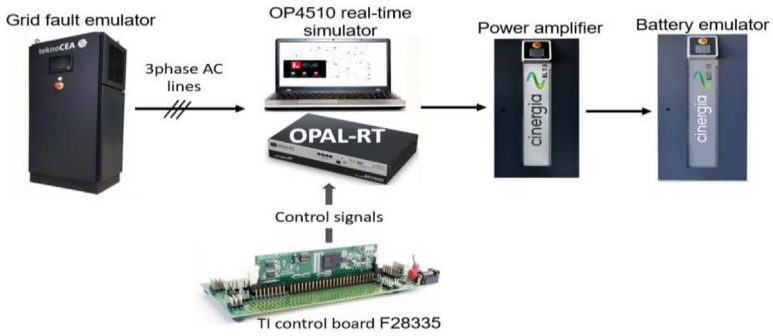

Fig. 15. Experimental test bench of the proposed charger.

simulator instead of the CPU core. The control will be implemented in the TI F28335 control board from Texas Instruments.

To test the control's effectiveness and the charger's adopted power structure, we will connect a battery emulator from Cinergia, as real batteries are not available for testing. The power amplifier from Cinergia will be used to adapt the output power from the simulator to the battery.

References

1 Thuttampatty Krishnamoorthy S., Vanitha Narayanan S., Kannan R. (2020) Real-time simulation of efficient energy management algorithms for electric vehicle chargers, in *Intelligent and efficient transport systems design, modelling, control and simulation*, T.Q. Dinh (ed.),IntechOpen, London, UK, pp. 113–131. Available at https://www.intechopen.com.

2 Drobnic K., Grandi G., Hammami M., Mandrioli R., Ricco M., Viatkin A., Vujacic M. (2019) An output ripple-free fast charger for electric vehicles based on grid-tied modular three-phase interleaved converters, *IEEE Trans. Ind. Appl.* **55**, 6, 6102–6114. https://doi.org/10.1109/TIA.2019.2934082.

3 Bayati M., Abedi M., Farahmandrad M., Gharehpetian G. B., Tehrani K. (2021) Important technical considerations in design of battery chargers of electric vehicles, *Energies (Basel)* **14**, 5878. https://doi.org/10.3390/en14185878.

4 Mądziel M., Campisi T. (2023) Energy consumption of electric vehicles: analysis of selected parameters based on created database, *Energies (Basel)* **16**, 3. https://doi.org/10.3390/en16031437.

5 Jaworski A., Mądziel M., Lew K., Campisi T., Woś P., Kuszewski H., Wojewoda P., Ustrzycki A., Balawender K., Jakubowski M. (2022) Evaluation of the effect of chassis dynamometer load setting on CO_2 emissions and energy demand of a full hybrid vehicle, *Energies* **15**, 1, 122. https://doi.org/10.3390/en15010122.

6 Town G., Taghizadeh S., Deilami S. (2022) Review of fast charging for electrified transport: demand, technology, systems, and planning, *Energies* **15**, 4, 1276. https://doi.org/10.3390/en15041276.

7 Ntombela M., Musasa K., Moloi K. (2023) A comprehensive review for battery electric vehicles (BEV) drive circuits technology, operations, and challenges, *World Electr. Veh. J.* **14**, 7, 195. https://doi.org/10.3390/WEVJ14070195.

8 Taghizad-Tavana K., Alizadeh A., Ghanbari-Ghalehjoughi M., Nojavan S. (2023) A comprehensive review of electric vehicles in energy systems: integration with renewable energy sources, charging levels, different types, and standards, *Energies* **16**, 2, 630. https://doi.org/10.3390/EN16020630.

9 Kumar S., Usman A., Rajpurohit B.S. (2021) Battery charging topology, infrastructure, and standards for electric vehicle applications: a comprehensive review, *IET Energy Syst. Integr.* **3**, 4, 381–396. https://doi.org/10.1049/ESI2.12038.

10 Arandhakar S., Jayaram N., Shankar Y.R., Gaurav, Kishore P.S.V., Halder S. (2022) Emerging intelligent bidirectional charging strategy based on recurrent neural network accosting EMI and temperature effects for electric vehicle, *IEEE Access* **10**, 121741–121761.https://doi.org/10.1109/ACCESS. 2022. 3223443.

11 Navas S.J., González G.M.C., Pino F.J., Guerra J.J. (2023) Modelling Li-ion batteries using equivalent circuits for renewable energy applications, *Energy Rep.* **9**, 4456–4465. https://doi.org/10.1016/J.EGYR.2023.03.103.

12 Bai H., Zhang Y., Semanson C., Luo C., Mi C.C. (2011) Modelling, design and optimisation of a battery charger for plug-in hybrid electric vehicles, *IET Electr. Sys. Transp.* **1**, 1, 3–10. https://doi.org/10.1049/iet-est.2010.0038.

13 Narasipuram R.P., Mopidevi S. (2023) "A novel hybrid control strategy and dynamic performance enhancement of a 3.3 kW GaN–HEMT-based iL2C resonant full-bridge DC–DC power converter methodology for electric vehicle charging systems, *Energies (Basel)* **16**, 15, 5811. https://doi.org/10.3390/en16155811.

14 Esfahani F.N., Darwish A., Williams B.W. (2022) Power converter topologies for grid-tied solar photovoltaic (PV) powered electric vehicles (EVs) – a comprehensive review, *Energies* **15**, 13, 4648. https://doi.org/10.3390/en15134648.

15 Ali A., Mousa H.H.H., Shaaban M.F., Azzouz M.A., Awad A. S.A. (2023) A comprehensive review on charging topologies and power electronic converter solutions for electric vehicles, *J. Mod. Power Syst. Clean Energy* 1–19. https://doi.org/10.35833/MPCE.2023.000107.

16 Safayatullah M., Elrais M.T., Ghosh S., Rezaii R., Batarseh I. (2022) A comprehensive review of power converter topologies and control methods for electric vehicle fast charging applications, *IEEE Access* **10**, 40753–40793. https://doi.org/10.1109/ACCESS.2022.3166935.

17 Chae B., Kang T., Kang T., Suh Y. (2015) Carrier based PWM for three-phase three-switch buck-type rectifier in EV rapid charging system, in 9th International Conference on Power Electronics – ECCE Asia: Green World with Power Electronics, ICPE 2015-ECCE Asia1–5 June, Seoul, Korea (South), IEEE, pp. 881–889. https://doi.org/10.1109/ICPE.2015.7167886.

18 Elserougi A., Abdelsalam I., Massoud A. (2022) An isolated-boost-converter-based unidirectional three-phase off-board fast charger for electric vehicles, *IET Electr. Syst. Transp.* **12**, 1, 79–88. https://doi.org/10.1049/ELS2.12039.

19 Rajendran G., Vaithilingam C.A., Naidu K., Oruganti K.S. P. (2020) Energy-efficient converters for electric vehicle charging stations, *SN Appl. Sci.* **2**, 4, 1–15. https://doi.org/10.1007/S42452-020-2369-0/TABLES/6.

20 Sweety P., Assistant J., Lakshmi M.M. (2021) Vienna rectifier for electric vehicle charging station, *Int. J. Mech. Eng.* **6**, 3, 974–5823.

21 Mohammed S.A.Q., Jung J.W. (2021) A comprehensive state-of-the-art review of wired/wireless charging technologies for battery electric vehicles: classification/common topologies/future research issues, *IEEE Access* **9**, 19572–19585. https://doi.org/10.1109/ACCESS.2021.3055027.

22 De Freige M. (2011) Design and simulation of a fast-charging station for plug-in hybrid electric vehicle (PHEV) batteries, *Thesis*. Available at https://escholarship.mcgill.ca/concern/theses/j098zg18r.

23 Acharige S.S.G., Haque M.E., Arif M.T., Hosseinzadeh N., Hasan K.N., Oo A.M.T. (2023) Review of electric vehicle charging technologies, standards, architectures, and converter configurations, *IEEE Access* 41218–41255. https://doi.org/10.1109/ACCESS.2023.3267164.

24 Nasir A., Hamad M.S., Elshenawy A.K. (2021) Design and development of a constant current constant voltage fast battery charger for electric vehicles, in 4th International Conference on Modern Research in Science, Engineering and Technology, 5–7, March, Berlin, Germany.

25 Yan Z., Yin Z., Yang X., Zhang K., Shi J., Wang L. (2018) Research and simulation of centralized charge and discharge technology of EVs based on MMC, in 2nd International Conference on Power and Renewable Energy (ICPRE), 20–23 September, Chengdu, China, IEEE, pp. 800–804. https://doi.org/10.1109/ICPRE.2017.8390644.

26 Ciccarelli F., Del Pizzo A., Iannuzzi D. (2013) An ultra-fast charging architecture based on modular multilevel converters integrated with energy storage buffers, in 8th International Conference and Exhibition on Ecological Vehicles and Renewable Energies (EVER), 7–30 March, Monte Carlo, Monaco. https://doi.org/10.1109/EVER.2013. 6521617.

27 Deng J., Li S., Hu S., Mi C.C., Ma R. (2014) Design methodology of LLC resonant converters for electric vehicle battery chargers, *IEEE Trans. Veh. Technol.* **63**, 4, 1581–1592. https://doi.org/10.1109/TVT.2013.2287379.

28 Valadkhani S., Mirsalim M., Gharehpetian G.B. (2021) Bidirectional isolated DC/DC dual-active-bridge converters optimum soft-switching control method for electrical vehicle applications, in 29th Iranian Conference on Electrical Engineering (ICEE), 18–20 May, Tehran, Iran, Islamic Republic of IEEE, pp. 363–367. https://doi.org/10.1109/ICEE52715.2021.9544312.

29 Chaurasiya S., Singh B. (2023) A bidirectional fast EV charger for wide voltage range using three-level DAB based on current and voltage stress optimization, *IEEE Trans. Transp. Electrif.* **9**, 1, 1330–1340. https://doi.org/10.1109/TTE.2022.3201979.

30 Naik N., Vyjayanthi C., Modi C. (2023) Filter-based active damping of DAB converter to lower battery degradation in EV fast charging application, *IEEE Access* **11**, 74277–74289. https://doi.org/10.1109/ACCESS.2023.3295988.

31 Mishra M., Sarkar I. (2023) EV battery charging using DAB DC-DC converter with EPS and DPS modulations, in IEEE International Students' Conference on Electrical, Electronics and Computer Science (SCEECS), 18–19 February, Bhopal, India. https://doi.org/10.1109/SCEECS57921.2023.10063090.

32 Deepak M., Janaki G., Bharatiraja C. (2023) Single phase shift dual active bridge high frequency DC-DC converter for electric vehicle battery charger 6.6 kW, in 5th International Conference on Electrical, Computer and Communication Technologies (ICECCT), 22–24, February, Erode, Tamil Nadu, India. https://doi.org/10.1109/ICECCT56650.2023.10179621.

33 Chen Z., Huang A.Q. (2024) Extreme high efficiency enabled by silicon carbide (SiC) power devices, *Mater. Sci. Semicond. Process* **172**, 108052. https://doi.org/10.1016/J.MSSP.2023.108052.

34 Naz H., Jamil M., Kirmani S. (2023) Real-time simulation of battery electric vehicle with PI controller tuned by particle swarm optimization (PSO) algorithm using OPAL-RT, in in International Conference on Power, Instrumentation, Energy and Control (PIECON), 10–12 February, Aligarh, India, IEEE. https://doi.org/10.1109/PIECON56912.2023.10085822.

35 Liu S., Xin D., Yang L., Li J., Wang L. (2020) A hierarchical V2G/G2V energy management system for electric-drive-reconstructed onboard converter, *IEEE Access* **8**, 198201–198213. https://doi.org/10.1109/ACCESS.2020.3034968.

36 Knez M., Zevnik G.K., Obrecht M. (2019) A review of available chargers for electric vehicles: United States of America, European Union, and Asia, *Renew. Sustain. Energy Rev.* **109**, 284–293. https://doi.org/10.1016/j.rser.2019. 04.013.

37 Duru K.K., Karra C., Venkatachalam P., Betha S.A., Anish Madhavan A., Kalluri S. (2021) Critical insights into fast charging techniques for lithium-ion batteries in electric vehicles, *IEEE Trans. Device Mater. Reliab.* **21**, 1, 137–152. https://doi.org/10.1109/TDMR.2021.3051840.

38 Mohanty A., Viswavandya M., Ray P.K., Mohanty S. (2018) Literature survey on OPAL-RT technologies with advance features and industrial applications, in 1st International Conference on Advanced Research in Engineering Sciences (ARES), 15 June, Dubai, United Arab Emirates, IEEE. https://doi.org/10.1109/ARESX. 2018.8723268.

39 Yoon H.M., Kim J.H., Song E.H. (2013) Design of a novel 50 kW fast charger for electric vehicles, *J. Cent. South Univ.* **20**, 2, 372–377. https://doi.org/10.1007/s11771-013-1497-8.

40 Rachid A., El Fadil H., Gaouzi K., Rachid K., Lassioui A., El Idrissi Z., Koundi M. (2023) Electric vehicle charging systems: comprehensive review, *Energies* **16**, 1, 255. https://doi.org/10.3390/en16010255.

41 Messaoudi H., Bourogaoui M., Ben Abdelghani A.B. (2022) Design of a smart and fast charger for electric vehicles, in IEEE International Conference on Electrical Sciences and Technologies in Maghreb (CISTEM)26–28 October, Tunis, Tunisia. https://doi.org/10.1109/CISTEM55808.2022.10043937.

42 Adaikkappan M., Sathiyamoorthy N. (2022) Modeling, state of charge estimation, and charging of lithium-ion battery in electric vehicle: a review, *Int. J. Energy Res.* **46**, 3, 2141–2165. https://doi.org/10.1002/er.7339.

43 Yilmaz M., Krein P.T. (2013) Review of battery charger topologies, charging power levels, and infrastructure for plug-in electric and hybrid vehicles, *IEEE Trans. Power Electron.* **28**, 5, 2151–2169. https://doi.org/10.1109/TPEL.2012.2212917.